Journal of Colloid and Interface Science 633 (2023) 1022–1032

Contents lists available at ScienceDirect

Journal of Colloid and Interface Science

journal homepage: www.elsevier.com/locate/jcis

Engineering adjacent N, P and S active sites on hierarchical porous carbon nanoshells for superior oxygen reduction reaction and rechargeable Zn-air batteries

Qingshan Zhao [a,1], Xiaojie Tan [a,1], Tengfei Liu [a], Shuai Hou [a], Wanxin Ni [a], Hao Huang [a], Jinqiang Zhang [b], Zhongxue Yang [a], Dawei Li [a], Han Hu [a], Mingbo Wu [a,*]

[a] State Key Laboratory of Heavy Oil Processing, College of Chemistry and Chemical Engineering, College of New Energy, China University of Petroleum (East China), Qingdao 266580, China
[b] School of Chemical Engineering and Advanced Materials, The University of Adelaide, Adelaide, SA 5005, Australia

HIGHLIGHTS

- Adjacent N, P and S-codoped hierarchical porous carbon nanoshells is fabricated through a layer-by-layer template coating strategy.
- The adjacent N, P and S dopants engineer synergistic and reinforced active sites for ORR.
- The metal-free catalyst exhibits superior activity, durability and methanol tolerance to the commercial Pt/C.
- The primary Zn-air battery delivers considerable open-circuit voltage, power density and long-term charge–discharge durability.

GRAPHICAL ABSTRACT

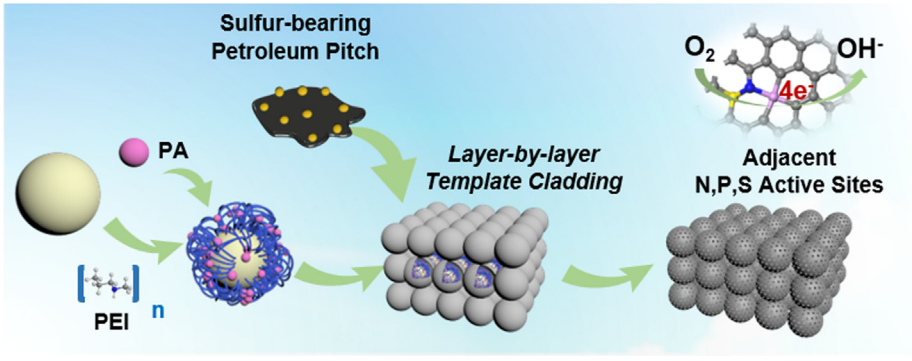

ARTICLE INFO

Article history:
Received 5 September 2022
Revised 26 November 2022
Accepted 28 November 2022
Available online 30 November 2022

Keywords:
Metal-free carbon-based catalyst
Heteroatom doping
Adjacent active site
Oxygen reduction reaction
Zn-air battery

ABSTRACT

Heteroatom-doped carbon materials have been regarded as sustainable alternatives to the noble-metal catalysts for oxygen reduction reaction (ORR), while the catalytic performances still remain unsatisfactory. Herein, we develop a metal-free adjacent N, P and S-codoped hierarchical porous carbon nanoshells (NPS-HPCNs) through a novel layer-by-layer template coating method. The NPS-HPCNs is rationally fabricated by crosslinking of polyethyenemine (PEI) and phytic acid (PA) on nano-SiO_2 template surface and subsequently coating of viscous sulfur-bearing petroleum pitch, followed by pyrolysis and alkaline etching. Soft X-ray absorption near-edge spectroscopy (XANES) analysis and density functional theory (DFT) calculations prove the engineering of adjacent N, P and S atoms to generate synergistic and reinforced active sites for oxygen electrocatalysis. The NPS-HPCNs manifests excellent ORR activity with a half-wave potential ($E_{1/2}$) of 0.86 V, as well as promoted durability and methanol tolerance in alkaline medium. Remarkably, the NPS-HPCNs-based Zn-air battery delivers an open-circuit voltage of 1.479 V, a considerable peak power density of 206 mW cm^{-2} and robust cycling stability (over 200 h), even exceeding the commercial Pt/C catalyst. This study offers fundamental insights into the construction and synergistic

* Corresponding author at: State Key Laboratory of Heavy Oil Processing, College of Chemistry and Chemical Engineering, College of New Energy, China University of Petroleum (East China), Qingdao 266580, Shandong, China.
E-mail address: wumb@upc.edu.cn (M. Wu).
[1] These authors contributed equally to this work.

https://doi.org/10.1016/j.jcis.2022.11.144

mechanism of adjacent heteroatoms on carbon substrate, providing advanced metal-free electrocatalysts for Zn-air batteries and other energy conversion and storage devices.

1. Introduction

Energy crisis and environmental degradation have attracted heightened attentions to develop renewable energy sources and green technologies, such as rechargeable metal-air batteries and regenerable fuel cells [1–2]. Especially, Zn-air battery is deemed as one of the most promising energy conversion technologies due to its high energy density, low cost and zero emission [3–6]. However, the high overpotential and sluggish kinetics of the cathodic oxygen reduction reaction (ORR) severely limit the energy efficiencies and power capabilities [7–10]. Although noble metal-based catalysts such as Pt/C exhibit excellent electrochemical activities toward ORR, the scarcity, high cost and intolerance to methanol severely hamper their extensive applications [11–12]. Therefore, developing efficient and cost-effective electrode materials to replace the noble metal electrocatalysts is of great significance.

A variety of synthetic methods have been proposed to construct efficient electrode materials for ORR, such as three-dimensional (3D) printing and joule heating [13–15]. Among them, metal-free carbon-based materials have been regarded as sustainable and promising substitutions to the noble-metal catalysts for ORR. Considering the intrinsic inertness of carbon, heteroatom doping is generally employed to create catalytic active sites on carbonaceous frameworks [16–18]. Theoretical and experimental investigations have demonstrated that heteroatom doping can readily break the electronic neutrality and change the charge and spin distribution of the carbon substrates, which benefits the O_2 adsorption and accelerates the ORR kinetics [19–21]. Especially, dual- or multi-heteroatom doping would further boost the ORR activity compared with mono-dopant, since multi-dopants could induce larger charge density changes or asymmetric spins of nearby carbon atoms [22–24]. For instance, Sun et al. deposited N, P-codoped graphene dots on *N*-doped (3D) graphene, leading to a good ORR activity with a half-wave potential ($E_{1/2}$) of 0.82 V in alkaline media [25]. Yang et al. developed a N, P and S tri-doped graphene-like carbon (NPS-G) derived from onium salts, resulting in an $E_{1/2}$ of 0.857 V for ORR, and an open-circuit voltage of 1.372 V and peak power density of 0.151 W cm^{-2} for Zn-air battery [26]. Nevertheless, heteroatom-doped carbon materials still exhibit unsatisfactory electrocatalytic performances for practical application in Zn-air batteries [23]. Especially, facile and reliable doping methods to realize the controllable location of heteroatom dopants, which is crucial to adjust the local charge distribution and synergistic catalytic effect, are extremely desirable to construct advanced metal-free electrocatalysts for ORR and Zn-air batteries.

Herein, we demonstrate a novel layer-by-layer template coating strategy to fabricate adjacent N, P and S-codoped hierarchical porous carbon nanoshells (NPS-HPCNs) as a superior electrocatalyst for ORR and rechargeable Zn-air batteries. By crosslinking polyethyenemine (PEI) with phytic acid (PA) over nano-SiO_2 template surface, followed by covering a layer of sulfur-bearing petroleum pitch, the NPS-HPCNs is rationally fabricated through carbonization and subsequent alkaline etching. With the advantages of mass production, low cost and abundance of aromatic compounds [27–28], the petroleum pitch is simultaneously employed as the carbon and sulfur sources, which facilitate the engineering of adjacent N, P and S active sites based on the layer-by-layer template coating strategy [29]. Owing to the synergistic and reinforced catalytic effect, as well as the hierarchical porous structure, the NPS-HPCNs shows superior electrocatalytic performance for ORR in alkaline medium. Interestingly, the primary Zn-air battery based on NPS-HPCNs delivers a considerable power density and long-term charge–discharge durability, even outperforming the commercial Pt/C catalyst.

2. Experimental

2.1. Materials

The petroleum pitch was obtained from the China National Petroleum Corporation (the composition and content are shown in Table S1). Polyethyenemine (PEI, MV = 1800), phytic acid (PA, 70 wt% solution), toluene (99 wt%), H_2SO_4 (98 wt%), KOH (95 wt %), NaOH (99 wt%), KSCN (99 wt%), K_2SO_4 (99 wt%), D-(+)-glucose, Nafion solution (5 wt%), 30 nm SiO_2 nanoparticles and 20 wt% Pt/C catalyst were purchased from Aladdin Biochemical Technology Co., ltd. The chemical reagents were used directly without further purification.

2.2. Synthesis of the electrocatalysts

50 mg PEI and 2 g SiO_2 nanoparticles (30 nm) were dispersed in water with stirring for 1 h. Then 800 mg PA was added into the solution and mixed evenly to crosslink with PEI on the SiO_2 template surface. The mixed solution was dried at 60 °C for one night, and the obtained powder was mixed with 500 mg petroleum pitch in 50 mL toluene solution. After intensive stirring, the solution was dried at 90 °C and subsequently carbonized at 900 °C for 3 h (with a heating rate of 5 °C min^{-1}) under N_2 atmosphere. The obtained sample was treated with 2 M NaOH at 90 °C for 12 h to remove the template. The precipitate was rinsed with deionized water to neutral and dried to obtain NPS-HPCNs.

N, S-doped and P, S-doped hierarchical porous carbon nanoshells (denoted as NS-HPCNs and PS-HPCNs) were prepared under the same condition without the addition of phosphorous source (PA) and nitrogen (PEI), respectively. N, P-doped hierarchical porous carbon nanoshells (NP-HPCNs) was also prepared by using glucose as the carbon source instead of petroleum pitch. Taken as controls, an isolated-NPS-HPCNs catalyst was prepared through a general template method by pyrolysis of PEI, PA, SiO_2 and petroleum pitch in one pot under the same conditions. NPS-HPCNs-NT was prepared in the absence of the SiO_2 template.

2.3. Material characterization

Scanning electron microscopy (SEM) images (Hitachi S-4800) and transmission electron microscopy (TEM) images (JEM-2100F) were captured to observe the microstructures and morphologies of NPS-HPCNs. The element distribution was evaluated by energy dispersive X-ray spectroscopy (EDX). Raman analysis was conducted on a Jobin-Yvon Labram-010 Raman spectrometer. X-ray photoelectron spectroscopy (XPS) investigation was performed on a Kratos Axis Ultra equipment (Chestnut Ridge) with Mg K_α radiation (1486.6 eV). The specific surface area and pore structure were measured by the Brunauer-Emmett-Teller (BET) method on a sorptometer (Micromeritics, ASAP 2020). The X-ray absorption near-edge structure (XANES) spectra were collected at the National Synchrotron Radiation Laboratory's BL12B beamlines (Beamlines

MCD-A and MCD-B (Soochow Beamline for Energy Materials)) (NSRL, Hefei). Electrochemical impedance spectroscopy (EIS) tests were conducted on a CHI760E electrochemistry workstation at a frequency range of 100 KHz to 10 MHz with an AC voltage amplitude of 5 mV.

2.4. Electrochemical measurements

Electrochemical measurements were performed on an electrochemical workstation (CHI 760E) with a three-electrode cell system, using an Ag/AgCl (saturated KCl) electrode as reference electrode and Pt wire as the counter electrode. All the potentials were referred to a reversible hydrogen electrode (RHE), $E_{RHE} = E_{Ag/AgCl} + 0.197\ V + 0.0591pH$. A rotating ring-disk electrode (RRDE) with a glassy carbon disk (GCE, 4 mm in diameter) and a Pt ring (with inner and outer diameters of 5 and 7 mm, respectively) was loaded with the as-prepared catalysts, serving as the working electrode. The morphology of the ring electrode is shown in Figure S1. 2 mg of samples were dispersed in 0.8 mL ethanol and 5 uL of 5 wt% Nafion solution under sonication for 30 min. 15 μL of the suspension was pipetted onto the GCE and dried in air at a catalyst loading of 0.30 mg cm^{-2}. Cyclic voltammetry (CV) tests were conducted in an O_2 saturated 0.1 M KOH electrolyte at a scan rate of 0.1 V s^{-1}. Linear-sweep voltammetry (LSV) measurements were performed at a scan rate of 5 mV s^{-1} under an electrode rotation rate of 1600 rpm. The applied potential at the ring electrode is 0.5 V.

The peroxide percentage (H_2O_2%) and the electron transfer number (n) are determined by the following equations:

$$H_2O_2\% = 200 \times (I_R/N)/(I_D + I_R/N) \quad (1\text{-}1)$$

$$n = 4 \times I_D/(I_D + I_R/N) \quad (1\text{-}2)$$

where I_D is the disk current, I_R is the ring current, and N is current collection efficiency of the Pt ring. N is determined to be 0.40.

The ORR tests were performed in an O_2 saturated 0.1 M KOH aqueous solution (70 mL). As to the methanol tolerance test, 47.5 μL methanol dissolved in 1 mL of 0.1 M KOH was added to the O_2-saturated 0.1 M KOH aqueous solution at 300 s.

2.5. Aqueous Zn-air battery tests

A primary Zn-air battery was assembled to verify the catalysts for application in energy conversion and storage devices. Polished zinc plate, 6 M KOH (containing 0.2 M $Zn(OAc)_2$) solution and carbon cloth loaded with 1 mg cm^{-2} catalyst were used as the negative electrode, electrolyte and positive electrode, respectively. Charge-discharge cycle experiments were carried out at 10 mA cm^{-2} for 30 min every cycle (15 mins charge, 15 mins discharge).

2.6. Density functional theory (DFT) calculations

Vienna Ab-initio Simulation Package was used to conduct all DFT calculations (VASP). The exchange correlation energy was computed using generalized gradient approximation (GGA) as parameterized by Perdew et al. based on the Perdew-Burke-Ernzerhof (PBE) functional [30–32]. In a plane wave basis with a kinetic cutoff energy of 500 eV, the Kohn-Sham orbitals were stretched. For graphite surfaces with unit cell of 5 × 5, Monkhorst-Pack meshes of 3 × 3 × 1k-point samplings in the surface Brillouin zones were chosen based on the lattice size. The Monkhorst-Pack meshes of 3 × 3 × 1k-point samplings in the surface Brillouin zones were used for the graphite surfaces with unit cell of 5 × 5. All of structures were completely relaxation. To eliminate periodic interactions, the 15 Å vacuum layer was used in the direction of the surface normal. For all computations, the optimization was converged until the stresses on each atom were less than 0.01 eV/Å and the overall energy differences were less than 10^{-6} eV.

3. Results and discussion

3.1. Catalyst synthesis and characterization

The NPS-HPCNs was rationally designed and fabricated through a novel layer-by-layer template coating method, as illustrated in Fig. 1a and Figure S2. Specifically, SiO_2 nanoparticles are firstly bonded and intertwined with the long-chain macromolecule of PEI. The abundant positive charged –NH and $–NH_2$ groups can further crosslink with the phosphate groups of PA (negative charged), resulting in a PEI-PA supermolecule layer covering over the surface of nano-SiO_2 template (Figure S3). The composite is further plastered with a layer of petroleum pitch with a sulfur content of 2.2 wt% (Table S1), achieving a layer-by-layer structure. N, P and S-codoped hierarchical porous carbon nanoshells can be facilely synthesized after carbonization and alkaline etching of the template. Remarkably, the layer-by-layer template coating strategy can efficiently arrange S speices in the petroleum pitch close to PEI (N source) and PA (P source), achieving adjacent N, P and S atoms on the carbon substrate as synergistic and reinforced active sites for ORR.

The morphology and structure of the samples were studied by SEM and TEM images, as shown in Fig. 1 and Figure S4. SEM images reveal the typical bulk structures both for the pristine petroleum pitch and NPS-HPCNs-NT in the absence of template (Fig. 1b and Fig. S4a-c). As expected, porous nanoshells characteristics appear on NPS-HPCNs after the template-oriented procedure with an inside diameter from 10 to 30 nm, indicating the pore-making effect of nano-SiO_2 templates (Fig. 1c, d). No residual nanoparticles can be observed on the carbon substrate, suggesting the completely removal of the SiO_2 template. SEM images of S-HPCNs, NS-HPCNs and PS-HPCNs demonstrate their similar porous hollow structure with NPS-HPCNs (Fig. S4d-i). Notably, some irregular fringes of amorphous carbon with a lattice distance of 3.5 Å can be seen in the HR-TEM image of NPS-HPCNs (Fig. 1e), and selected-area electron diffraction further confirms the amorphous structure of the sample (Figure S5). TEM image (Fig. 1f) and corresponding EDX elemental mapping images (Fig. 1g) of NPS-HPCNs manifest the homogeneous distribution of N, P and S elements over the substrate, implying the successful introduction of N, P and S atoms uniformly distributed on the carbon frameworks.

XRD patterns of the heteroatom-doped carbon materials are illustrated in Fig. 2a. All of S-HPCNs, PS-HPCNs, NS-HPCNs and NPS-HPCNs exhibit two obvious peaks centered at around 26° and 44°, which belong to the (002) and (100) diffraction of graphitic materials, respectively. The broad peaks suggest emerged defects and disorders in the carbon structure after the introduction of heteroatoms [33]. Compared with S-HPCNs and NS-HPCNs, the (002) peaks of PS-HPCNs and NPS-HPCNs move to lower diffraction angles, indicating the larger lattice spacing within carbon layer caused by the intercalation of P atoms with bigger atomic radius [34]. The structural changes were further confirmed by Raman analysis. Two peaks at around 1350 cm^{-1} (D band) and 1595 cm^{-1} (G band) can be found in Fig. 2b, and the intensity ratio of D and G bands (I_D/IG) represents the degree of structural order [35]. Owing to the easy graphitization property, S-HPCNs directly derived from petroleum pitch shows a low I_D/IG of 0.86. In comparison, the I_D/IG ratios of PS-HPCNs and NPS-HPCNs increase to 0.88 and 0.89, respectively, indicating more defects induced by heteroatom doping. Whereas NS-HPCNs shows the highest I_D/IG of 0.99 among the samples, which might be ascribed to the instability of

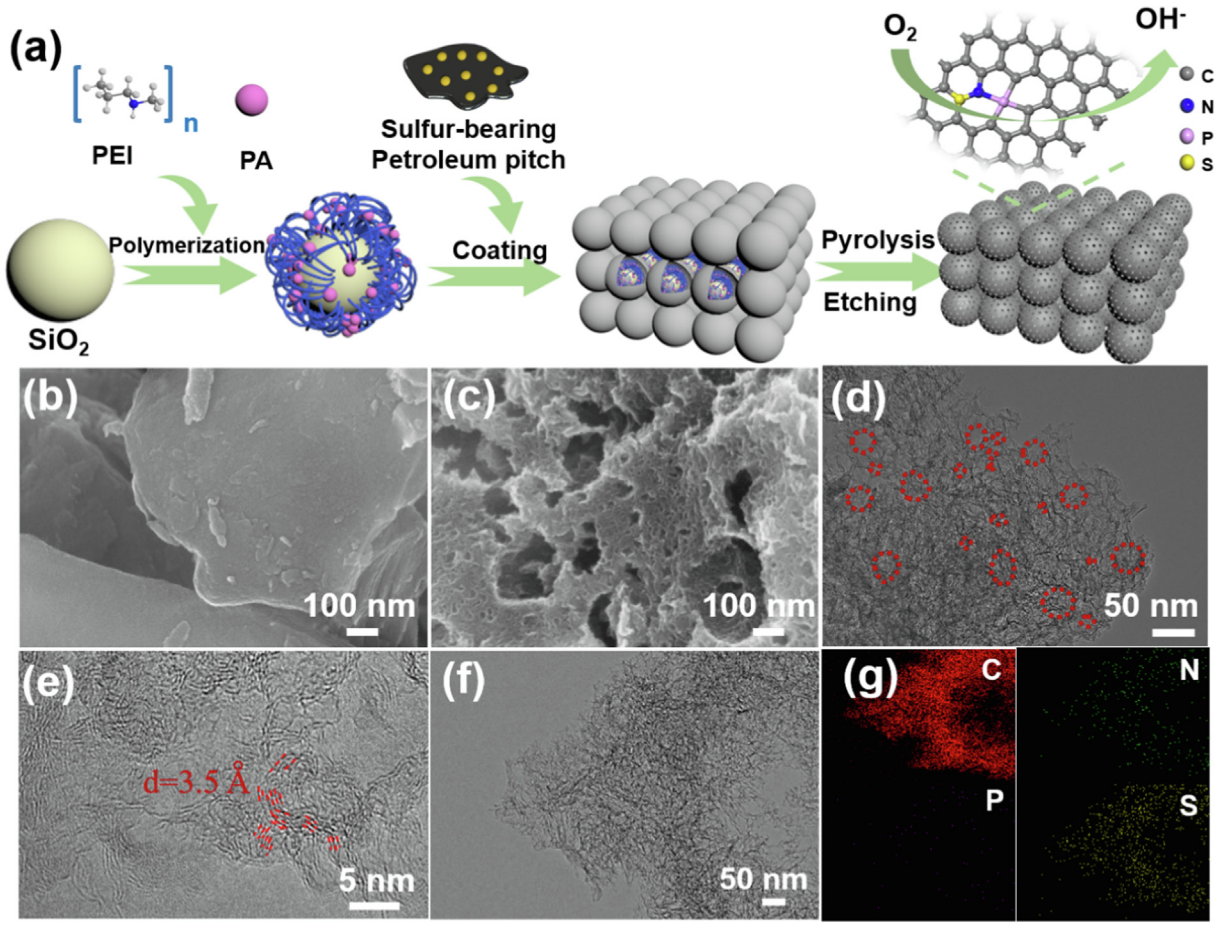

Fig. 1. Schematic illustration of the preparation procedure for NPS-HPCNs (a). SEM images of petroleum pitch (b) and NPS-HPCNs (c). TEM (d) and HR-TEM (e) images of NPS-HPCNs. TEM image of NPS-HPCNs (f) and corresponding EDX elemental mapping of C, N, P and S (g).

PEI during thermal treatment to generate more structural disorder/defects. Notably, all the samples exhibit a broad 2D band at around 2691 cm^{-1}, (D + G) band at around 2935 cm^{-1} and 2D' band at around 3192 cm^{-1}, indicating the high graphitization degree to establish conductive networks for electron transport [36]. The porous nanostructure and pore size distribution were further determined by N_2 adsorption/desorption isotherm measurements. S-HPCNs, NS-HPCNs, PS-HPCNs and HPCNs all exhibit type IV isotherms with hysteresis loops, with a surface area of 929, 734, 565 and 715 m^2 g^{-1}, respectively (Fig. 2c). Pore size distribution analysis reveals the coexistence of micropores, mesopores and macropores in all samples (Fig. 2d). The micropores should be generated resulted from the released gas species in the pyrolysis procedure, while the mesopores and macropores may originate from the pore-making effect of the template. Compared with S-HPCNs, the relative smaller surface area of NS-HPCNs, PS-HPCNs and NPS-HPCNs should be attributed to the destruction of partial mesopores caused by the released gas from PA and PEI polymers. Such hierarchical porous structure with high surface area would provide accessible mass transfer pathways to the active sites in the oxygen electrocatalysis process [37].

The chemical composition of the prepared samples was investigated by XPS measurements. As shown in Fig. 3a, C, N, O and S elements can be found in the spectrum of S-HPCNs, with an additional N signal in NS-HPCNs, P signal in PS-HPCNs, and N and P signals in NPS-HPCNs. The contents of N, P and S in NPS-HPCNs are determined to be 1.0 ± 0.1, 0.3 ± 0.1 and 1.1 ± 0.3 at.%, respectively (Table S2). C 1 s XPS spectra of the samples can be deconvoluted into three peaks at 284.5, 286.5 and 288.1 eV, corresponding to C═C, C—O/C═N/C—P and O-C═O, respectively (Fig. 3b). The high percentage of sp^2-hybridized carbon reflects the graphitized structure of NPS-HPCNs. In terms of the S 2p XPS spectra, S-HPCNs and PS-HPCNs show peaks at the binding energy of 163.5, 164.8 and 167.8 eV, respectively (Fig. 3c). The former two peaks are assigned to $2p_{3/2}$ and $2p_{1/2}$ of thiophenic S (C—S—C), and the latter peak is responsible for oxidized S (C-SO_x-C) species. By comparison, slight shifts occur on the S $2p_{3/2}$ peaks of NS-HPCN and NPS-HPCNs, with an additional peak emerging at 164.2 eV, suggesting the formation of S—N bond and charge transfer from adjacent N and P atoms. Two peaks at 130.9 and 133.9 eV corresponding to P—C and P—O bonds can be seen in the P 2p XPS spectrum of NPS-HPCs (Figure S6). This verifies the successful doping of P atoms into the carbon lattice, whose 3d orbitals can modulate the local charge density and regulate the lone pair electrons of O_2 to trigger ORR [38]. N 1s spectra reveals five peaks at 398.1, 399.5, 400.4, 401.6 and 405.7 eV assigned to pyridinic N, N—S, pyrrolic N, graphitic N, and pyridinic-*N*-oxide species, respectively (Fig. 3d) [39]. It is worth mentioning that the introduced oxygen should be derived from the petroleum pitch source (Figure S7), which can facilitate the contact between the electrolyte and electrode. Particularly, due to adjacent S and P doping, NPS-HPCNs affords an enlarged proportion of graphitic N compared with NS-HPCNs, which can donate more p electrons to the π system of the carbon substrate to create efficient active sites for ORR [40].

Soft X-ray absorption near-edge spectroscopy (XANES), a reliable technique to unveil the local chemical environment and elec-

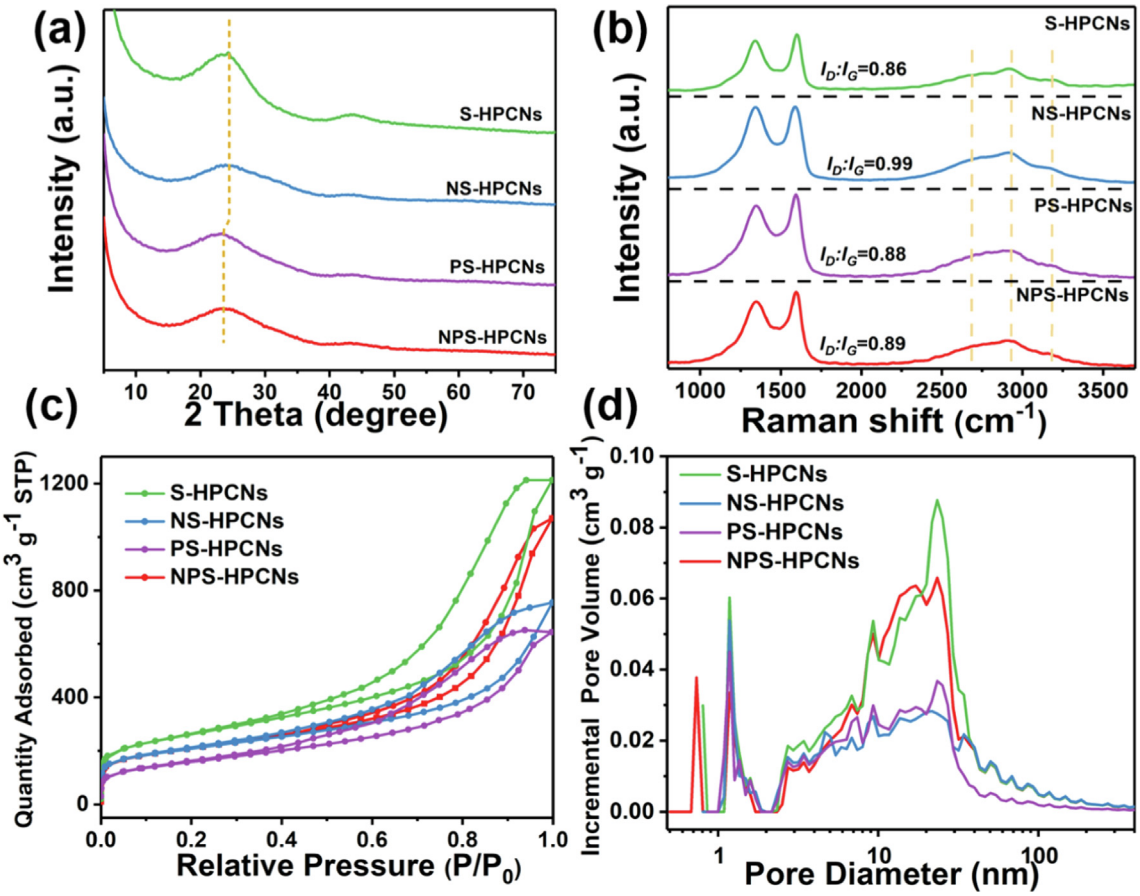

Fig. 2. XRD patterns (a) and Raman spectra (b) of S-HPCNs, NS-HPCNs, PS-HPCNs and NPS-HPCNs. N_2 adsorption/desorption isotherms (c) and the pore size distribution (d) of S-HPCNs, NS-HPCNs, PS-HPCNs and NPS-HPCNs.

tronic structure, was further conducted to gain insight into the atomic interaction among C, S, N and P atoms. As shown in Fig. 4a, the C K-edge spectra are dominated by two strong peaks centered at 285.5 and 292.4 eV, corresponding to the excitation of C 1s electrons to the π*C═C and σ*C—C orbitals, respectively. Besides, all the samples exhibit a peak centered at 289.6 eV assigned to π*C—S—C orbitals, while additional peaks at 288.1 (π*C—N—C orbitals) and 288.4 eV (π*C—P—C) orbitals can be found in NS-HPCNs and PS-HPCNs, respectively. Although all the peaks can be observed in NPS-HPCNs, the intensity of π*C═C and σ*C—C peaks show simultaneously declines, confirming the chemical interaction induced by N, P and S dopants [41]. The S L-edge XANES spectra present three peaks at around 164.0, 165.4 and 166.9 eV classified to C—S—C coordination species (Fig. 4b). Notably, compared with S-HPCNs, the middle peaks in NS-HPCNs, NP-HPCNs and NPS-HPCNs show a gradual upshift, indicating that S is positively charged by adjacent N and P atoms due to their higher electronegativity [42]. Furthermore, the electronic states of N in NS-HPCNs and NPS-HPCNs were detected by the N K-edge XANES spectra. As shown in Fig. 4c, the peaks at around 399.4, 402.8 and 408.0 eV are attributed to pyridinic N, pyrrolic N and graphitic N, respectively. Compared with NS-HPCNs, the stronger intensities of pyridinic N and graphitic N species of NPS-HPCNs reveal the introduction of more pyridinic N and graphitic N species, which can be beneficial to the transportation of O_2 to the active sites and facilitate the 4-electron ORR process (Fig. 4c). Fig. 4d displays the P L-edge XANES spectra for PS-HPCNs and NPS-HPCNs. The peak at 146.5 eV corresponds to the 2p to 3p transitions of P atom, and the peak at 142.3 eV is attributed to the P—C/N bonds, demonstrating the well intercalation of P. The above XANES results provide strong evidence for the formation of adjacent N, P and S atoms on the carbon skeletons to construct highly efficient active sites for ORR.

3.2. Electrocatalytic performance towards ORR

The prepared samples were utilized as ORR catalysts to evaluate their electrocatalytic performance. S-HPCNs, NS-HPCNs, PS-HPCNs, NP-HPCNs, NPS-HPCNs and NPS-HPCNs-NT samples were firstly performed in 0.1 M KOH solution saturated with N_2 or O_2 for cyclic voltammetry (CV) tests. It can be clearly observed in Fig. 5a and Figure S9a that all the samples exhibit cathodic peaks in O_2-saturated solution, illustrating the effective electrochemical O_2 reduction. Among all the catalysts, NPS-HPCNs displays the most conspicuous cathodic peak and highest peak intensity, suggesting its superior ORR activity to other samples. Linear sweep voltammetry (LSV) measurements were determined to further evaluate the ORR performance using RRDE at 1600 rpm (Fig. 5b). The NPS-HPCNs shows an onset potential (E_{onset}) of 0.96 V (vs RHE) and a half wave potential ($E_{1/2}$) of 0.86 V (vs RHE), which is even comparable to that of Pt/C catalyst, with E_{onset} of 0.99 V and $E_{1/2}$ of 0.86 V, respectively. Based on the E_{onset} and $E_{1/2}$ results, the ORR activity of ternary doped NPS-HPCNs is significantly improved compared with S-HPCNs and the co-doped samples (NS-HPCNs and PS-HPCNs), and is much higher than NP-HPCNs and NPS-HPCNs-NT (Figure S9b), indicating that ternary doping of N, P and S poses a promotion effect on the ORR performance. A control isolated-NPS-HPCNs catalyst was prepared through a general template

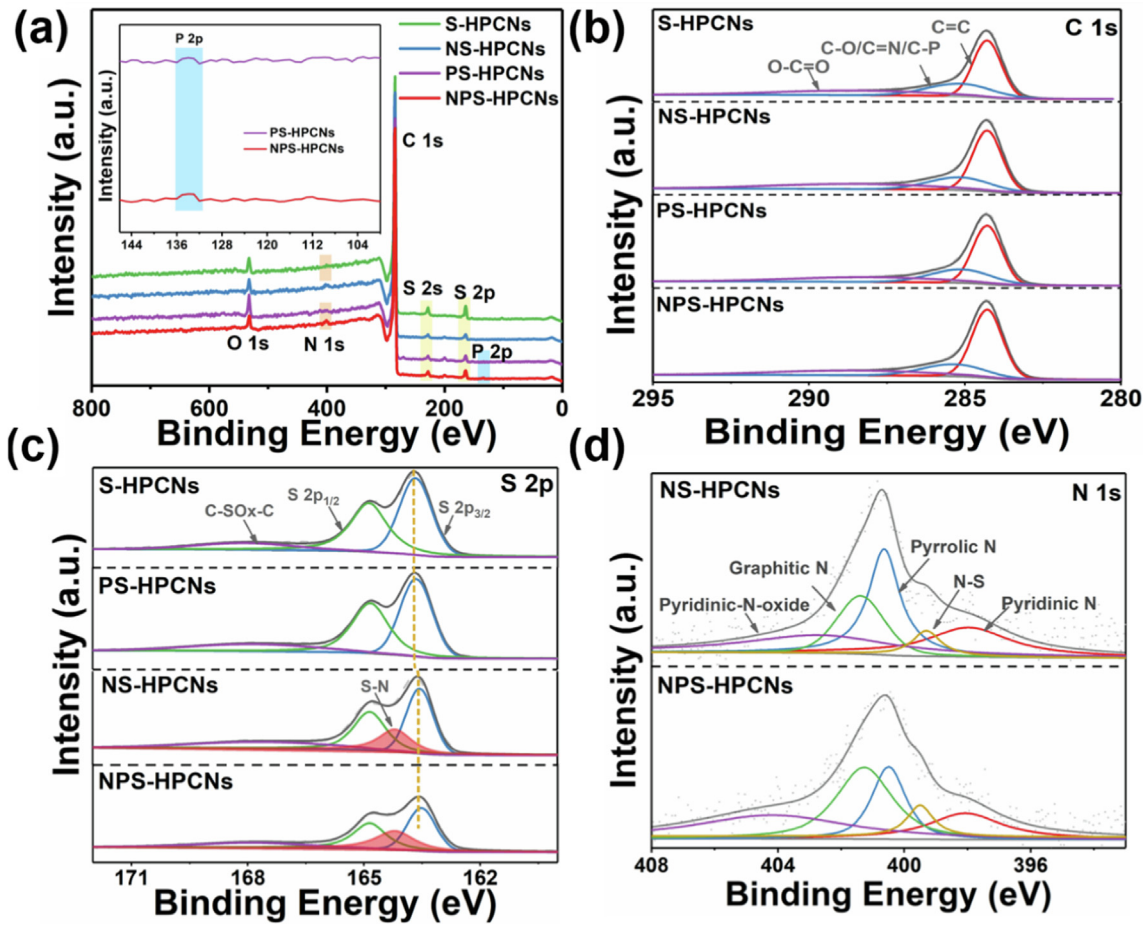

Fig. 3. XPS survey spectra of S-HPCNs, NS-HPCNs, PS-HPCNs and NPS-HPCNs (a). The inset is a local magnification from 100 to 146 eV. C 1s (b) and S 2p (c) XPS spectra of S-HPCNs, NS-HPCNs, PS-HPCNs and NPS-HPCNs. N 1s XPS spectra of NS-HPCNs and NPS-HPCNs (d).

method by pyrolysis of PEI, PA, SiO_2 and petroleum pitch in one pot. It can be determined that without the layer-by-layer strategy, the isolated-NPS-HPCNs catalyst displays a much worse ORR activity than NPS-HPCNs, as concluded by the CV and LSV results in Figure S10. The results confirm the synergy effect of adjacent N, P and S atoms on modulation of charge spin density and delocalization of carbon atoms, constructing superior active sites for ORR [43]. Figure S11 presents the CV and LSV results of NPS-HPCNs samples dependent on the pyrolysis temperature, among which NPS-HPCNs-900 stands out. The results reveal that pyrolysis temperature would affect the heteroatom doping manner and degree of graphitization, which significantly influence the ORR performance.

The Tafel plots of the catalysts calculated from mass transfer correction of related LSV data are shown in Fig. 5c. NPS-HPCNs exhibits a Tafel slope of 72.54 mV Dec^{-1}, which is much smaller than commercial Pt/C (91.80 mV Dec^{-1}) and other doped-carbon catalysts, indicating a faster reaction kinetics of ORR. The electrochemically active surface area (ECSA) of NPS-HPCNs was measured based on double layer capacitance (C_{dl}) in the non-Faradaic potential region (Figure S12). According to the CV measurements at various scan rates, C_{dl} is calculated to be 5.63 mF cm^{-2}. And the ECSA of NPS-HPCNs is calculated to be 0.18 mA cm^{-2}_{ECSA}. Electrochemical impedance spectroscopy (EIS) test of NPS-HPCNs shows a small semicircle at the high-frequency region and a line with high slope at the low-frequency region, indicating the low interfacial charge transfer resistance and rapid ion diffusion across the catalyst (Figure S13). Therefore, the hierarchical porous hollow structure and adjacent N, P and S dopants guarantee more accessible contact between the dissolved O_2 and efficient active sites. LSV of the samples were recorded with rotation rate ranged from 400 rpm to 2500 rpm, and the ORR kinetics was analyzed by the Kouteckye-Levich (K-L) plots based on K-L equations (Figure S14-15). All the prepared catalysts follow the first-order reaction with respect to the dissolved O_2. The electron transfer numbers (n) of S-HPCNs, NS-HPCNs, PS-HPCNs, NPS-HPCNs and Pt/C are calculated to be 2.35, 2.78, 2.88, 3.92 and 4.01, respectively. The average n of NPS-HPCNs is calculated to be 3.95 under the potential window from 0.2 to 0.5 V, with an average H_2O_2 yield below 4.4 % (Figure S16), demonstrating a four-electron pathway on NPS-HPCNs.

Fig. 5e shows the LSV curves of NPS-HPCNs before and after 3000 cycles. NPS-HPCNs shows an excellent electrocatalytic ORR stability, with a slight negative shift of $E_{1/2}$ from 0.86 to 0.85 V. The stability was further investigated through amperometric i-t measurements (Figure S17). The commercial Pt/C catalyst shows a gradual fading of current density within 12 h and results in a retention rate of 70 %. Remarkably, the NPS-HPCNs displays an outstanding durability, with a reinforced retention rate of 93 %, indicating an enhanced stability of the metal-free NPS-HPCNs than commercial Pt/C catalyst. SEM of NPS-HPCNs after the long-term electrochemical tests was carried out, which still remains the porous structure, indicating its robust structural stability (Figure S18). Moreover, methanol tolerance ability is a crucial factor on the practical application of ORR electrocatalysts. As such, methanol crossover tests were carried out (Fig. 5f). When methanol was injected at the interval time of 300 s, the Pt/C catalyst suffers a significant decrease on current density, while the impact of methanol on the ORR electrocatalytic performance of NPS-HPCNs is minimal, indicating its exceptional methanol tolerance capability. To further

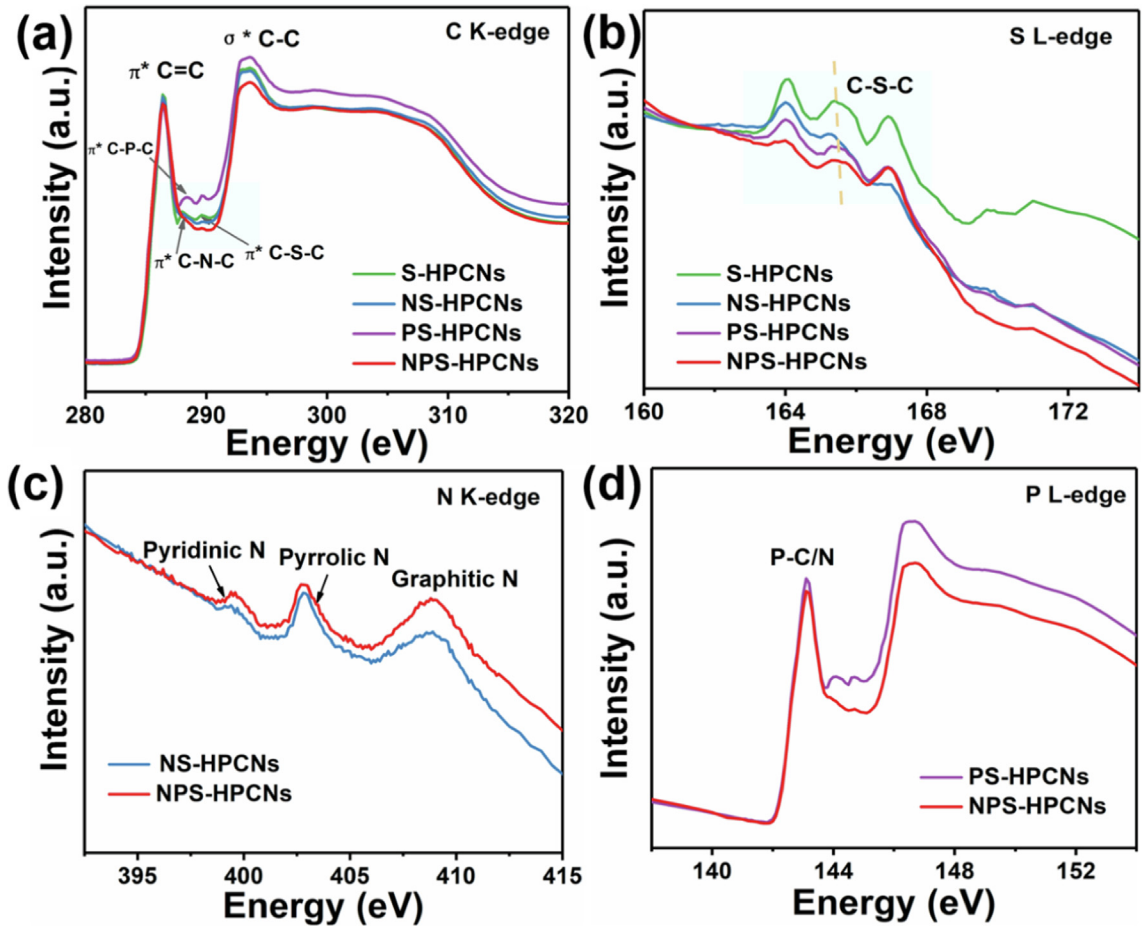

Fig. 4. C K-edge (a) and S L-edge (b) XANES spectra of S-HPCNs, NS-HPCNs, PS-HPCNs and NPS-HPCNs. N K-edge XANES spectra of NS-HPCNs and NPS-HPCNs (c). P L-edge XANES spectra of PS-HPCNs and NPS-HPCNs (d).

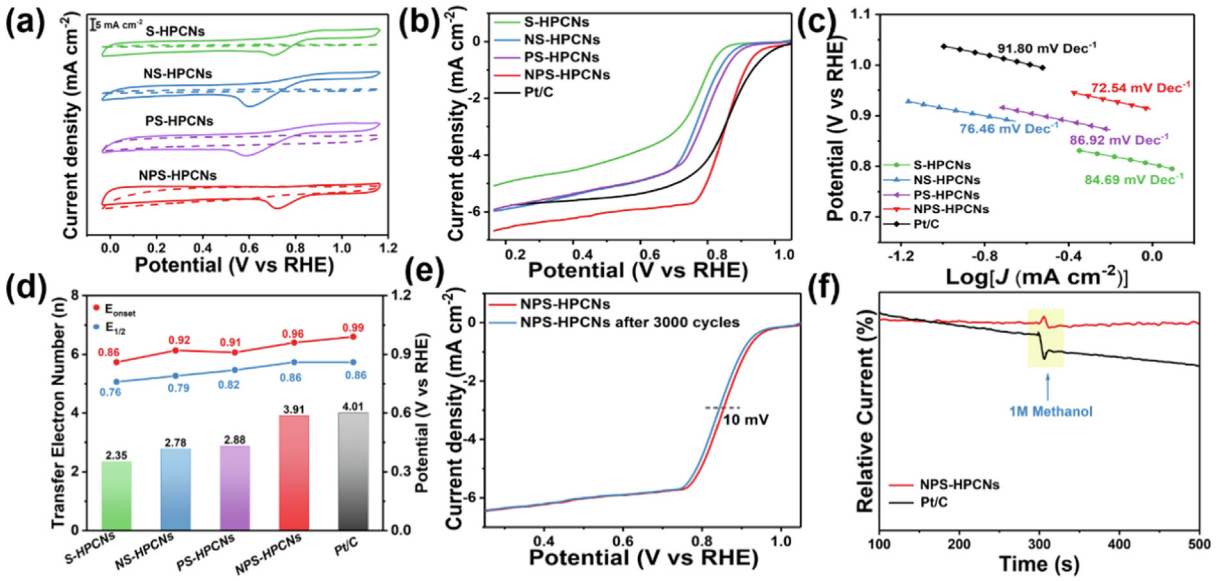

Fig. 5. CV curves of S-HPCNs, NS-HPCNs, PS-HPCNs and NPS-HPCNs in N_2 (dashed curves) or O_2 (solid curves)-saturated 0.1 M KOH solution (a). LSV curves of S-HPCNs, NS-HPCNs, PS-HPCNs, NPS-HPCNs and commercial Pt/C (20 wt%) in O_2-saturated 0.1 M KOH solution at a rotating speed of 1600 rpm (b). Tafel plots of the catalysts derived from mass transport correction of corresponding LSV data (c). E_{onset}, $E_{1/2}$ and n for the catalysts (d). LSV curves of NPS-HPCNs before and after 3000 cycles (e). Methanol tolerance tests of NPS-HPCNs and Pt/C (f).

evaluate the stability against environmental factors, the NPS-HPCNs was respectively pretreated under acid, base, high temperature and high humidity conditions. As shown in Figure S19, it can be found that the metal-free catalyst exhibits excellent tolerance against the above conditions, which shows hardly activity change or slight performance decrease for ORR.

3.3. Rechargeable zinc-air batteries

Motivated by the extraordinary ORR electrochemical performance of NPS-HPCNs, its effectiveness as an air–cathode for Zn-air batteries was investigated. A primary Zn-air battery was assembled with a carbon cloth supported electrocatalyst working as the air cathode and a 6 M KOH solution containing 0.2 M $Zn(OAc)_2$ as the electrolyte (Fig. 6a). As can be seen in Fig. 6b, three batteries in series with NPS-HPCNs as the air cathode can work properly and readily power a light-emitting diode (LED) screen. As shown in Fig. 6c, the initial open-circuit voltage of the NPS-HPCNs-based Zn-air battery is tested to be 1.479 V, which is higher than 1.401 V of Pt/C catalyst. Fig. 6d and Figure S20 displays the polarization and power density curves for the Zn-air batteries. Obviously, compared with S-HPCNs, NS-HPCNs, PS-HPCNs and NP-HPCNs, the NPS-HPCNs-based Zn-air battery exists a prominent peak power density of 206 mW cm^{-2}, exceeding the commercial Pt/C catalyst (135 mW cm^{-2}). The NPS-HPCNs also exhibits superior charging and discharging abilities to the commercial Pt/C catalyst in rechargeable Zn-air batteries (Figure S21), demonstrating its reliable electrocatalytic activities. Moreover, the galvanostatic discharge voltages of NPS-HPCNs and Pt/C both decrease with the increasing of current densities (Fig. 6f). Besides, the NPS-HPCNs-based Zn-air battery shows voltage plateaus of 1.37, 1.34, 1.33, 1.32. 1.31 and 1.29 V at the discharge current densities of 1, 3, 5, 7, 10 and 15 mA cm^{-2}, respectively, which are higher than those of Pt/C catalyst. Remarkably, the NPS-HPCNs-based battery delivers reinforced charge and discharge potentials in a 200 h long-term cycling test at a current density of 10 mA cm^{-2}, indicating its satisfactory electrocatalytic performance for rechargeable Zn-air batteries (Fig. 6g). To explore the effect of foreign ions on the performance of NPS-HPCNs in Zn-air batteries, the catalyst was pre-impregnated in SO_4^{2-}, Na^+ and SCN^- solutions, respectively. As shown in Figure S22, the various foreign ions show negligible influences on the performance of the batteries, suggesting prominent ion tolerance and reinforced stability of the metal-free active sites.

3.4. Density functional theory calculations

Density functional theory (DFT) calculations were conducted to elucidate the synergetic mechanism of the adjacent heteroatoms on the carbon substrate. Combined with the XPS and XANES results, two NPS-HPCNs models with adjacent N, P and S dopants

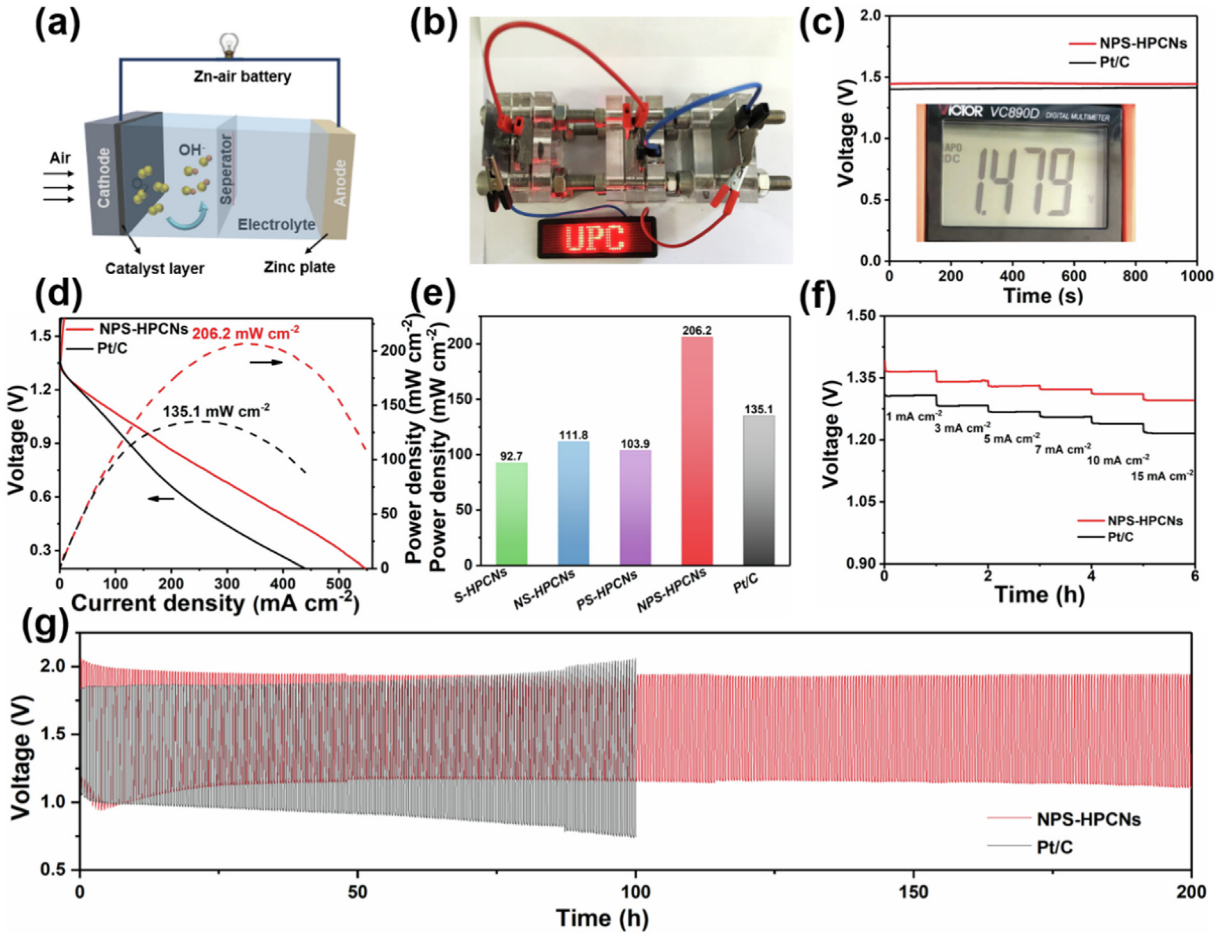

Fig. 6. Graphical illustration for the Zn-air battery (a). Photograph of red LED screen powered by three NPS-HPCNs-based Zn-air batteries in series (b). Initial open-circuit potential (c) and polarization curves and corresponding power density plots (d) of Zn-air batteries with NPS-HPCNs and Pt/C as the air cathodes. The peak power density for S-HPCNs, NS-HPCNs, PS-HPCNs, NP-HPCNs, NPS-HPCNs and Pt/C-based Zn-air batteries (e). Discharge profiles of the Zn-air batteries using NPS-HPCNs and Pt/C as the air-catalyst at current densities of 1, 2, 5, 7, 10 and 15 mA cm^{-2} (f). Long-term cycling performance of the Zn-air batteries at a current density of 10 mA cm^{-2} (g). (For interpretation of the references to colour in this figure legend, the reader is referred to the web version of this article.)

were constructed. Figure S23 shows the top view of optimized adsorption configurations of the reaction intermediates (*OOH, *O and *OH) adsorbed on the model surfaces. Apparently, the first model displays much lower free energy barriers during the reaction pathway, revealing the optimal configuration of NPS-HPCNs. Bader charge analysis and charge density change of the optimal NPS-HPCNs model indicate inhomogeneous local charge distribution and obvious charge transfer between the adjacent N, P and S atoms, forming effective active sites for ORR (Figure S24). Furthermore, the optimized adsorption configurations and free energy reaction pathway for NS-HPCNs, PS-HPCNs, NP-HPCNs, NPS-HPCNs and isolated-NPS-HPCNs are also conducted (Figure S25 and Fig. 7a-b). Due to the charge modulation effect arising from surroudning N and S atoms, O_2 molecule is favorable to be adsorbed on the P sites. Under the equilibrium potential of ORR (U = 1.23 V vs RHE), the first reduction step ($O_2 \rightarrow$ *OOH) and last reduction step ($OH^* \rightarrow H_2O$) are uphill over the catalysts except for NP-HPCNs, suggesting an applied potential to overcome the positive free energy change [44]. Among all the samples, NPS-HPCNs shows the smallest ΔG of 0.25 eV for the hydrogenation of O_2 to *OOH and relatively low energy barrier of 0.69 eV for the protonation step of OH*, indicating its strengthened catalytic efficiency [45]. To validate the effect of heteroatom location on the catalytic reactions, free energy reaction pathway over isolated-NS-HPCNs and isolated-NPS-HPCNs were also investigated. As shown in Figure S26 and Fig. 7c, the contrastive samples with isolated heteroatom dopants need to overcome much higher energy barriers compared with NS-HPCNs and NPS-HPCNs, accounting for their inferior ORR catalytic activities. The calculation results manifest the reinforced synergistic effect of adjacent N, P and S active sites for ORR electrocatalysis, which can significantly promote the adsorption of O_2 and reduce the energy barriers, leading to superior electrocatalytic performance for ORR and rechargeable Zn-air batteries (Figure S27).

Based on the experimental and theoretical results, the NPS-HPCNs exhibits a prominent electrocatalytic activity for ORR and outstanding power density and rechargeable stability for as the cathode for Zn-air batteries. The outstanding performance of NPS-HPCNs should be mainly attributed to the following factors. Firstly, adjacent N, P and S atoms are controllably engineered based on the layer-by-layer template coating strategy, which uneven the local charge distribution of the carbon substrates to generate reinforced synergistic active sites, significantly accelerate the adsorption of O_2 and reduce the energy barriers of ORR. Secondly, the hierarchical porous hollow structure, as well as the high graphitization degree of the carbon matrix, provide more rapid mass and electron transferring channels towards the active sites, smoothly facilitating the proceeding of electrocatalytic ORR. Moreover, the excellent structural stability of the metal-free active sites ensures the superior durability for ORR and reversibility for rechargeable Zn-air batteries, demonstrating its great potential for practical applications.

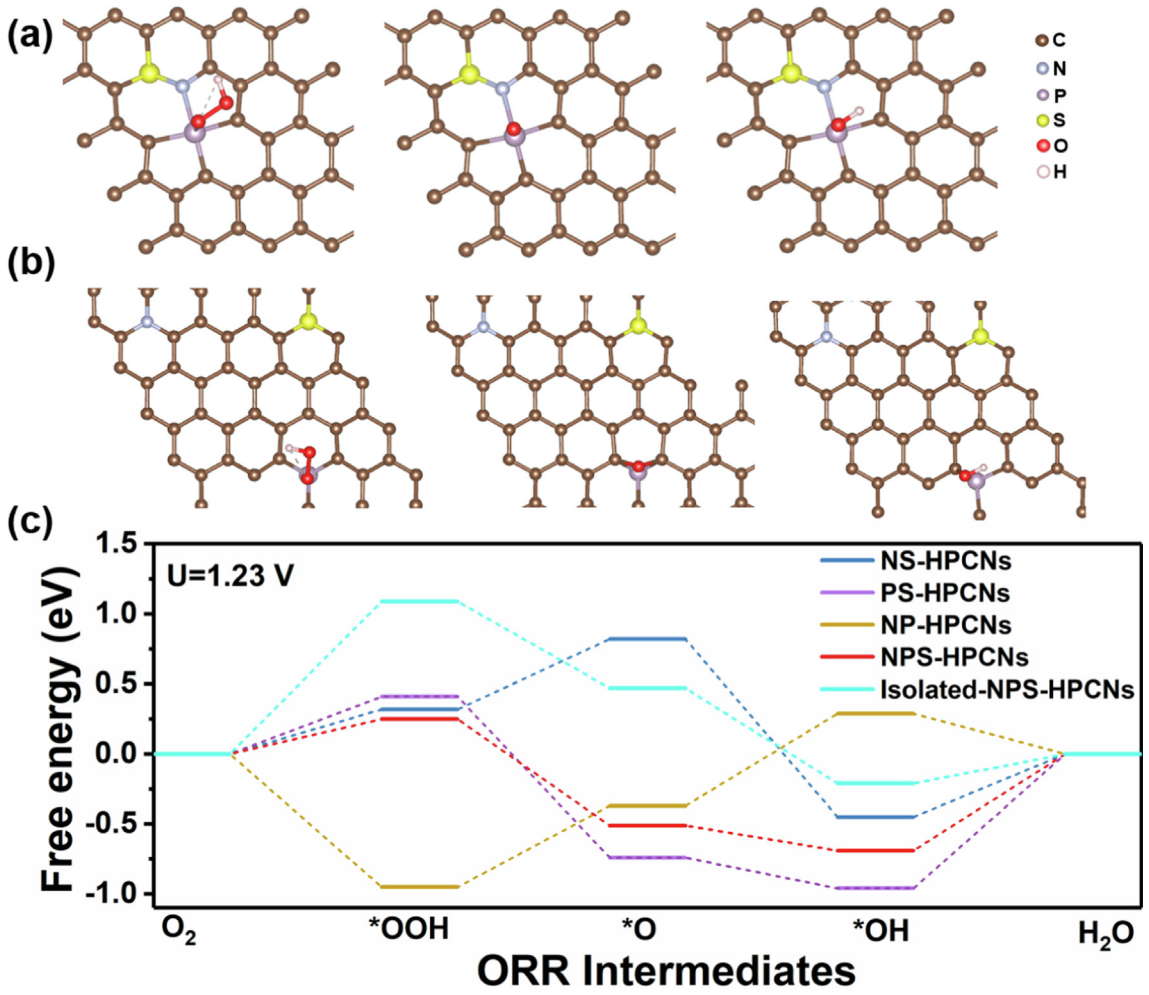

Fig. 7. The proposed absorption geometry of oxygen intermediates (*OOH, *O, *OH) on NPS-HPCNs (a) and isolated-NPS-HPCNs (b). Free energy diagram for the four-electron oxygen reduction pathway on NS-HPCNs, PS-HPCNs, NP-HPCNs, NPS-HPCNs and isolated-NPS-HPCNs in alkaline media at U = 1.23 V (c).

4. Conclusion

In summary, we have successfully developed a novel layer-by-layer template coating strategy for the fabrication of adjacent N, P and S atoms on hierarchical porous carbon nanoshells. The hierarchical porous hollow structure can facilitate mass transport and electron transfer during the electrocatalytic process. The adjacent N, P and S atoms engineer synergistic and reinforced active sites that can dramatically promote the adsorption of O_2 and reduce the energy barriers for ORR. These advantages endow NPS-HPCNs with superior catalytic performances for ORR and Zn-air batteries, standing out among the recently reported metal-free catalysts (Table S3-4). The NPS-HPCNs shows excellent electrochemical activity for ORR with an $E_{1/2}$ of 0.86 V, reinforced durability and methanol tolerance. The Zn-air battery based on NPS-HPCNs cathode delivers an exceptional open-circuit voltage of 1.479 V, a considerable peak power density of 206 mW cm^{-2} and a good cycling stability for over 200 h, even outperforming the commercial Pt/C catalyst. Based on these findings, this study provides fresh insights into the construction and synergistic mechanism of adjacent heteroatoms on carbon substrate, achieving advanced electrodes for rechargeable Zn-air batteries and other energy conversion and storage devices.

CRediT authorship contribution statement

Qingshan Zhao: Conceptualization, Writing – review & editing, Funding acquisition. **Xiaojie Tan:** Investigation, Methodology, Data curation, Writing – original draft. **Tengfei Liu:** Investigation, Methodology, Writing – original draft. **Shuai Hou:** Software, Methodology. **Wanxin Ni:** Investigation, Data curation. **Hao Huang:** Writing – original draft, Formal analysis. **Jinqiang Zhang:** Methodology, Validation. **Zhongxue Yang:** Formal analysis, Data curation. **Dawei Li:** Writing – review & editing. **Han Hu:** Resources, Project administration. **Mingbo Wu:** Writing – review & editing, Supervision, Funding acquisition.

Data availability

Data will be made available on request.

Declaration of Competing Interest

The authors declare that they have no known competing financial interests or personal relationships that could have appeared to influence the work reported in this paper.

Acknowledgments

The authors are grateful for the XAENS tests assisted by Prof. Jun Bao and Jiawei Xue from the University of Science and Technology of China. This work is financially supported by the National Natural Science Foundation of China (No. 22208375, 2213000238), China; the National Key R&D Program of China (No. 2019YFA0708700), China; the Shandong Provincial Natural Science Foundation (No. ZR2019QB016, ZR2018ZC1458), China; the financial support from Taishan Scholar Project of Shandong Province of China (No. ts201712020), China; Technological Leading Scholar of 10000 Talent Project (No. W03020508), China.

Appendix A. Supplementary material

Supplementary data to this article can be found online at https://doi.org/10.1016/j.jcis.2022.11.144.

References

[1] R.F. Service, Zinc aims to beat lithium batteries at storing energy, Science 372 (2021) 890–891, 10.1126/science.372.6545.890.
[2] E. Luo, Y. Chu, J. Liu, Z. Shi, S. Zhu, L. Gong, J. Ge, C.H. Choi, C. Liu, W. Xing, Pyrolyzed M-N_x catalysts for oxygen reduction reaction: progress and prospects, Energ. Environ. Sci. 14 (2021) 2158–2185, https://doi.org/10.1039/d1ee00142f.
[3] M. Wu, G. Zhang, M. Wu, J. Prakash, S. Sun, Rational design of multifunctional air electrodes for rechargeable Zn-air batteries: recent progress and future perspectives, Energy Storage Mater. 21 (2019) 253–286, https://doi.org/10.1016/j.ensm.2019.05.018.
[4] X. Zhu, C. Hu, R. Amal, L. Dai, X. Lu, Heteroatom-doped carbon catalysts for zinc-air batteries: progress, mechanism, and opportunities, Energ. Environ. Sci. 13 (2020) 4536–4563, https://doi.org/10.1039/d0ee02800b.
[5] T. Zhou, N. Zhang, C. Wu, Y. Xie, Surface/interface nanoengineering for rechargeable Zn–air batteries, Energ. Environ. Sci. 13 (2020) 1132–1153, https://doi.org/10.1039/c9ee03634b.
[6] W. Zhang, Y.P. Chen, L. Zhang, J.J. Feng, X.S. Li, A.J. Wang, Theophylline-regulated pyrolysis synthesis of nitrogen-doped carbon nanotubes with iron-cobalt nanoparticles for greatly boosting oxygen reduction reaction, J. Colloid Interf. Sci. 626 (2022) 653–661, https://doi.org/10.1016/j.jcis.2022.06.130.
[7] S.S. Shinde, J.Y. Jung, N.K. Wagh, C.H. Lee, D.-H. Kim, S.-H. Kim, S.U. Lee, J.-H. Lee, Ampere-hour-scale zinc–air pouch cells, Nat. Energy 6 (2021) 592–604, https://doi.org/10.1038/s41560-021-00807-8.
[8] S. Ren, X. Duan, S. Liang, M. Zhang, H. Zheng, Bifunctional electrocatalysts for Zn-air batteries: recent developments and future perspectives, J. Mater. Chem. A 8 (2020) 6144–6182, https://doi.org/10.1039/c9ta14231b.
[9] C. Han, W. Li, H.K. Liu, S. Dou, J. Wang, Principals and strategies for constructing a highly reversible zinc metal anode in aqueous batteries, Nano Energy 74 (2020), https://doi.org/10.1016/j.nanoen.2020.104880 104880.
[10] J.-T. Ren, Y.-S. Wang, L. Chen, L.-J. Gao, W.-W. Tian, Z.-Y. Yuan, Binary FeNi phosphides dispersed on N, P-doped carbon nanosheets for highly efficient overall water splitting and rechargeable Zn-air batteries, Chem. Eng. J. 389 (2020), https://doi.org/10.1016/j.cej.2020.124408 124408.
[11] K. Kodama, T. Nagai, A. Kuwaki, R. Jinnouchi, Y. Morimoto, Challenges in applying highly active Pt-based nanostructured catalysts for oxygen reduction reactions to fuel cell vehicles, Nat. Nanotechnol. 16 (2021) 140–147, https://doi.org/10.1038/s41565-020-00824-w.
[12] Y. Yuan, J. Wang, S. Adimi, H. Shen, T. Thomas, R. Ma, J.P. Attfield, M. Yang, Zirconium nitride catalysts surpass platinum for oxygen reduction, Nat. Materials 19 (2020) 282–286, https://doi.org/10.1038/s41563-019-0535-9.
[13] X. Tian, K. Zhou, 3D printing of cellular materials for advanced electrochemical energy storage and conversion, Nanoscale 12 (2020) 7416–7432, https://doi.org/10.1039/d0nr00291g.
[14] W. Zhang, X. Liao, X. Pan, M. Yan, Y. Li, X. Tian, Y. Zhao, L. Xu, L. Mai, Superior hydrogen evolution reaction performance in 2H-MoS_2 to that of 1T phase, Small 15 (2019) e1900964.
[15] D. Xi, J. Li, J. Low, K. Mao, R. Long, J. Li, Z. Dai, T. Shao, Y. Zhong, Y. Li, Z. Li, X.J. Loh, L. Song, E. Ye, Y. Xiong, Limiting the uncoordinated N species in M-N_x single-atom catalysts toward electrocatalytic CO_2 reduction in broad voltage range, Adv. Mater. 34 (2022) 2104090, https://doi.org/10.1002/adma.202104090.
[16] T.T. Xiang, Z.R. Wu, Z.T. Sun, C. Cheng, W.L. Wang, Z.Z. Liu, J. Yang, B. Li, The synergistic effect of carbon edges and dopants towards efficient oxygen reduction reaction, J. Colloid Interface Sci. 610 (2022) 486–494, https://doi.org/10.1016/j.jcis.2021.11.069.
[17] L.X. Cui, J.Y. Zhao, G.S. Liu, Z.Y. Wang, B. Li, L.B. Zong, Rich edge-hosted single-atomic Cu-N_4 sites for highly efficient oxygen reduction reaction performance, J. Colloid Interface Sci. 622 (2022) 209–217, https://doi.org/10.1016/j.jcis.2022.04.098.
[18] Z.W. Fan, X.J. Cui, J.K. Wei, C. Chen, H.L. Tang, J.S. Li, Host-guest interactions promoted formation of Fe-N-4 active site toward efficient oxygen reduction reaction catalysis, J. Colloid Interface Sci. 621 (2022) 195–204, https://doi.org/10.1016/j.jcis.2022.04.059.
[19] X. Huang, T. Shen, S. Sun, Y. Hou, Synergistic modulation of carbon-based, precious-metal-free electrocatalysts for oxygen reduction reaction, ACS Appl. Mater. Inter. 13 (2021) 6989–7003, https://doi.org/10.1021/acsami.0c19922.
[20] H.W. Kim, V.J. Bukas, H. Park, S. Park, K.M. Diederichsen, J. Lim, Y.H. Cho, J. Kim, W. Kim, T.H. Han, J. Voss, A.C. Luntz, B.D. McCloskey, Mechanisms of two-Electron and four-electron electrochemical oxygen reduction reactions at nitrogen-doped reduced graphene oxide, ACS Catal. 10 (2019) 852–863, https://doi.org/10.1021/acscatal.9b04106.
[21] H. Li, M. Zhang, W. Zhou, J. Duan, W. Jin, Ultrathin 2D catalysts with N-coordinated single Co atom outside Co cluster for highly efficient Zn-air battery, Chem. Eng. J. 421 (2021), https://doi.org/10.1016/j.cej.2021.129719 129719.
[22] Z. Xu, L. Li, X. Chen, G. Xiao, N, S-codoped mesoporous carbons derived from polymer micelle-based assemblies for the oxygen reduction reaction, ACS Appl. Energ. Mater. 4 (2021) 1954–1961, https://doi.org/10.1021/acsaem.0c03075.
[23] L. Yang, J. Shui, L. Du, Y. Shao, J. Liu, L. Dai, Z. Hu, Carbon-based metal-free ORR electrocatalysts for fuel cells: past, present, and future, Adv. Mater. 31 (2019) 1804799, https://doi.org/10.1002/adma.201804799.
[24] H.L. Meng, S.Y. Lin, J.J. Feng, L. Zhang, A.J. Wang, Coordination regulated pyrolysis synthesis of ultrafine FeNi/$(FeNi)_{(9)}S_8$ nanoclusters/nitrogen, sulfur-

codoped graphitic carbon nanosheets as efficient bifunctional oxygen electrocatalysts, J. Colloid Interface Sci. 610 (2022) 573–582, https://doi.org/10.1016/j.jcis.2021.11.101.
[25] X. Tong, M. Cherif, G. Zhang, X. Zhan, J. Ma, A. Almesrati, F. Vidal, Y. Song, J.P. Claverie, S. Sun, N, P-codoped graphene dots supported on N-doped 3D graphene as metal-free catalysts for oxygen reduction, ACS Appl. Mater. Inter. 13 (2021) 30512–30523, https://doi.org/10.1021/acsami.1c03141.
[26] Y. Wang, N. Xu, R. He, L. Peng, D. Cai, J. Qiao, Large-scale defect-engineering tailored tri-doped graphene as a metal-free bifunctional catalyst for superior electrocatalytic oxygen reaction in rechargeable Zn-air battery, Appl. Catal. B: Environ. 285 (2021), https://doi.org/10.1016/j.apcatb.2020.119811 119811.
[27] H. Hu, M. Wu, Heavy oil-derived carbon for energy storage applications, J. Mater. Chem. A 8 (2020) 7066–7082, https://doi.org/10.1039/d0ta00095g.
[28] T. Ma, X. Tan, Q. Zhao, Z. Wu, F. Cao, J. Liu, X. Wu, H. Liu, X. Wang, H. Ning, M. Wu, Template-oriented synthesis of Fe–N-codoped graphene nanoshells derived from petroleum pitch for efficient nitroaromatics reduction, Ind. Eng. Chem. Res. 59 (2019) 129–136, https://doi.org/10.1021/acs.iecr.9b06072.
[29] Q. Zhao, X. Tan, T. Ma, F. Cao, Z. Xia, H. Liu, H. Ning, Z. Li, H. Hu, M. Wu, Reinforced atomically dispersed FeNC catalysts derived from petroleum asphalt for oxygen reduction reaction, J. Colloid Interface Sci. 587 (2021) 810–819, https://doi.org/10.1016/j.jcis.2020.11.040.
[30] P. John, K.B. Perdew, Matthias Ernzerhof, Generalized gradient approximation made simple, Phys. Rev. Lett., 77 (1996) 3865-3868, 10.1103/PhysRevLett.77.3865.
[31] G. Kresse, D. J., From ultrasoft pseudopotentials to the projector augmented-wave method. Phys. Rev. B, 59 (1999) 1758-1775, 10.1103/PhysRevB.59.1758.
[32] G. KresseaJ, F.,, Efficiency of ab-initio total energy calculations for metals and semiconductors using a plane-wave basis set, Comp. Mater. Sci. 6 (1996) 15–50, https://doi.org/10.1016/0927-0256(96)00008-0.
[33] K.A. Raj, M.R. Panda, D.P. Dutta, S. Mitra, Bio-derived mesoporous disordered carbon: an excellent anode in sodium-ion battery and full-cell lab prototype, Carbon 143 (2019) 402–412, 10.1016/j.carbon.2018.11.038.
[34] S. Yang, X. Mao, Z. Cao, Y. Yin, Z. Wang, M. Shi, H. Dong, Onion-derived N, S self-doped carbon materials as highly efficient metal-free electrocatalysts for the oxygen reduction reaction, Appl. Surf. Sci. 427 (2018) 626–634, https://doi.org/10.1016/j.apsusc.2017.08.222.
[35] A.A. King, B.R. Davies, N. Noorbehesht, P. Newman, T.L. Church, A.T. Harris, J.M. Razal, A.I. Minett, A new Raman metric for the characterisation of graphene oxide and its derivatives, Sci. Rep. 6 (2016) 19491, https://doi.org/10.1038/srep19491.
[36] C. Zhao, Q. Wang, Y. Lu, B. Li, L. Chen, Y.-S. Hu, High-temperature treatment induced carbon anode with ultrahigh Na storage capacity at low-voltage plateau, Sci. Bull. 63 (2018) 1125–1129, https://doi.org/10.1016/j.scib.2018.07.018.
[37] Y. Wang, L. Tao, Z. Xiao, R. Chen, Z. Jiang, S. Wang, 3D carbon electrocatalysts in situ constructed by defect-rich nanosheets and polyhedrons from NaCl-sealed zeolitic imidazolate frameworks, Adv. Funct. Mater. 28 (2018) 05356, https://doi.org/10.1002/adfm.201705356.
[38] Z. Xing, R. Jin, X. Chen, B. Chen, J. Zhou, B. Tian, Y. Li, D. Fan, Self-templating construction of N, P-co-doped carbon nanosheets for efficient eletreocatalytic oxygen reduction reaction, Chem. Eng. J. 410 (2021), https://doi.org/10.1016/j.cej.2020.128015 128015.
[39] J.S. Stevens, S.J. Byard, C.C. Seaton, G. Sadiq, R.J. Davey, S.L. Schroeder, Proton transfer and hydrogen bonding in the organic solid state: a combined XRD/XPS/ssNMR study of 17 organic acid-base complexes, PCCP 16 (2014) 1150–1160, https://doi.org/10.1039/c3cp53907e.
[40] Q. Lv, N. Wang, W. Si, Z. Hou, X. Li, X. Wang, F. Zhao, Z. Yang, Y. Zhang, C. Huang, Pyridinic nitrogen exclusively doped carbon materials as efficient oxygen reduction electrocatalysts for Zn-air batteries, Appl. Catal. B: Environ. 261 (2020), https://doi.org/10.1016/j.apcatb.2019.118234 118234.
[41] H. Shang, X. Zhou, J. Dong, A. Li, X. Zhao, Q. Liu, Y. Lin, J. Pei, Z. Li, Z. Jiang, D. Zhou, L. Zheng, Y. Wang, J. Zhou, Z. Yang, R. Cao, R. Sarangi, T. Sun, X. Yang, X. Zheng, W. Yan, Z. Zhuang, J. Li, W. Chen, D. Wang, J. Zhang, Y. Li, Engineering unsymmetrically coordinated Cu-S_1N_3 single atom sites with enhanced oxygen reduction activity, Nat. Commun. 11 (2020) 3049, https://doi.org/10.1038/s41467-020-16848-8.
[42] P. Chen, N. Zhang, S. Wang, T. Zhou, Y. Tong, C. Ao, W. Yan, L. Zhang, W. Chu, C. Wu, Y. Xie, Interfacial engineering of cobalt sulfide/graphene hybrids for highly efficient ammonia electrosynthesis, PANS 116 (2019) 6635–6640, https://doi.org/10.1073/pnas.1817881116.
[43] J. Zhang, Z. Zhao, Z. Xia, L. Dai, A metal-free bifunctional electrocatalyst for oxygen reduction and oxygen evolution reactions, Nat. Nanotechnol. 10 (2015) 444–452, https://doi.org/10.1038/nnano.2015.48.
[44] Z. Zhu, H. Yin, Y. Wang, C.H. Chuang, L. Xing, M. Dong, Y.R. Lu, G. Casillas-Garcia, Y. Zheng, S. Chen, Y. Dou, P. Liu, Q. Cheng, H. Zhao, Coexisting single-atomic Fe and Ni sites on hierarchically ordered porous carbon as a highly efficient ORR electrocatalyst, Adv. Mater. 32 (2020) 2004670, https://doi.org/10.1002/adma.202004670.
[45] Y. Wang, Z. Li, P. Zhang, Y. Pan, Y. Zhang, Q. Cai, S.R.P. Silva, J. Liu, G. Zhang, X. Sun, Z. Yan, Flexible carbon nanofiber film with diatomic Fe-Co sites for efficient oxygen reduction and evolution reactions in wearable zinc-air batteries, Nano Energy 87 (2021), https://doi.org/10.1016/j.nanoen.2021.106147 106147.